Atomic Structure and Electron Magnetic Circular Dichroism of Individual Rock Salt Structure Antiphase Boundaries in Spinel Ferrites

Zhuo Li, Jinlian Lu, Lei Jin, Ján Rusz, Vancho Kocevski, Hideto Yanagihara, Eiji Kita, Joachim Mayer, Rafal E. Dunin-Borkowski, Hongjun Xiang,* and Xiaoyan Zhong*

Spinel ferrites are an important class of materials, whose magnetic properties are of interest for industrial applications. The antiphase boundaries (APBs) that are commonly observed in spinel ferrite films can hinder their applications in spintronic devices and sensors, as a result of their influence on magnetic degradation and magnetoresistance of the materials. However, it is challenging to correlate magnetic properties with atomic structure in individual APBs due to the limited spatial resolution of most magnetic imaging techniques. Here, aberration-corrected scanning transmission electron microscopy and electron energy-loss magnetic chiral dichroism are used to measure the atomic structure and electron magnetic circular dichroism (EMCD) of a single APB in $NiFe_2O_4$ that takes the form of a rock salt structure interlayer and is associated with a crystal translation of $(1/4)a$[011]. First principles density functional theory calculations are used to confirm that this specific APB introduces antiferromagnetic coupling and a significant decrease in the magnitude of the magnetic moments, which is consistent with an observed decrease in EMCD signal at the APB. The results provide new insight into the physical origins of magnetic coupling at an individual defect on the atomic scale.

1. Introduction

Spinel ferrites have a wide spectrum of magnetic properties. They have attracted attention for their utilization in sensors, transformers, antennas, high-frequency inductors, microwave devices, and spintronic devices.[1] Antiphase boundaries (APBs), which are commonly observed in spinel ferrite films, can contribute to magnetoresistance,[2] increase the critical field for magnetic saturation,[3] and cause local magnetic degradation,[4] which can be deleterious for applications. It is therefore important to understand interface configurations and magnetic coupling across individual APBs. Atomic models of APBs have been constructed on the basis of their crystallographic relationships and verified experimentally using dark-field transmission electron microscopy (TEM)

Z. Li, Dr. X. Zhong
National Center for Electron Microscopy in Beijing
Key Laboratory of Advanced Materials (MOE)
The State Key Laboratory of New Ceramics and Fine Processing
School of Materials Science and Engineering
Tsinghua University
Beijing 100084, China
E-mail: xzhong25@cityu.edu.hk

Z. Li, Dr. X. Zhong
Department of Materials Science and Engineering
City University of Hong Kong
Tat Chee Avenue, Kowloon, Hong Kong 999077, China

Z. Li, Dr. X. Zhong
Shenzhen Futian Research Institute
City University of Hong Kong
Shenzhen 518048, P. R. China

The ORCID identification number(s) for the author(s) of this article can be found under https://doi.org/10.1002/adfm.202008306.

Z. Li, Dr. X. Zhong
Nanomanufacturing Laboratory (NML)
Shenzhen Research Institute
City University of Hong Kong
Shenzhen 518057, China

Dr. J. Lu, Prof. H. Xiang
Key Laboratory of Computational Physical Sciences
(Ministry of Education)
State Key Laboratory of Surface Physics
and Department of Physics
Fudan University
Shanghai 200433, China
E-mail: hxiang@fudan.edu.cn

Dr. J. Lu
Department of Physics
Yancheng Institute of Technology
Yancheng 224051, China

Dr. L. Jin, Prof. J. Mayer, Prof. R. E. Dunin-Borkowski
Ernst Ruska-Centre for Microscopy and Spectroscopy with Electrons
Forschungszentrum Jülich GmbH
52425 Jülich, Germany

Dr. J. Rusz, Dr. V. Kocevski
Department of Physics and Astronomy
Uppsala University
P.O. Box 516, Uppsala S-75120, Sweden

**ADVANCED
SCIENCE NEWS**
www.advancedsciencenews.com

**ADVANCED
FUNCTIONAL
MATERIALS**
www.afm-journal.de

and high-resolution scanning TEM (STEM).[5] Domains that are on either side of an APB are typically related to each other by a crystallographic translation of the form $(1/4)a[110]$ or $(1/2)a[100]$, where a is the lattice parameter. Only the cation sublattice is then shifted, with the oxygen sublattice remaining more or less undisturbed.[5b,c] The atomic structure of an APB is sometimes more complicated, for example, if the two shifted domains are not connected directly but are separated by an interlayer. Such configurations have rarely been studied in detail.

The atomic-scale structures and nanoscale magnetic properties of the same APBs or twin boundaries can be studied by using a combination of aberration-corrected (S)TEM with phase contrast techniques such as off-axis electron holography,[6] Lorentz microscopy,[7] and differential phase contrast imaging.[8] However, element-specific magnetic information, which is important for complex oxides such as spinel ferrites, is then missing. In addition, it is difficult to investigate non-conductive materials using phase contrast techniques, as a result of the influence of electron-beam-induced specimen charging. An alternative powerful technique for imaging magnetic microstructure in a (S)TEM that has element specificity is electron energy-loss magnetic chiral dichroism,[9] which is also referred to as electron magnetic circular dichroism (EMCD). This technique is similar to X-ray magnetic circular dichroism (XMCD),[10] in that it permits the quantitative element-selective measurement of spin and orbital magnetic moment in materials from spectra measured at core-loss edges.[11] When it is implemented using convergent electron beam illumination, the spatial resolution of EMCD can reach a few nm,[12] or even the sub-nm scale.[13]

Here, we study an APB with a rock salt structure interlayer in inverse spinel $NiFe_2O_4$. In contrast to commonly-observed APBs, high-angle annular dark-field (HAADF) STEM imaging is used to show that the two shifted domains, which have a relative translation of $(1/4)a[011]$, are separated by a rock salt structure interlayer in which only half of the octahedral interstices are occupied. Quantitative analysis of EMCD spectra recorded under optimized dynamical diffraction conditions reveals a significant decrease in experimental EMCD strength at the APB, as compared to that in the adjacent perfect domains. Dynamical diffraction simulations and first-principles density functional theory (DFT) calculations are used to investigate how the atomic structure of the APB affects magnetic coupling within it and to determine the magnetic moments of the constituent Fe and Ni cations.
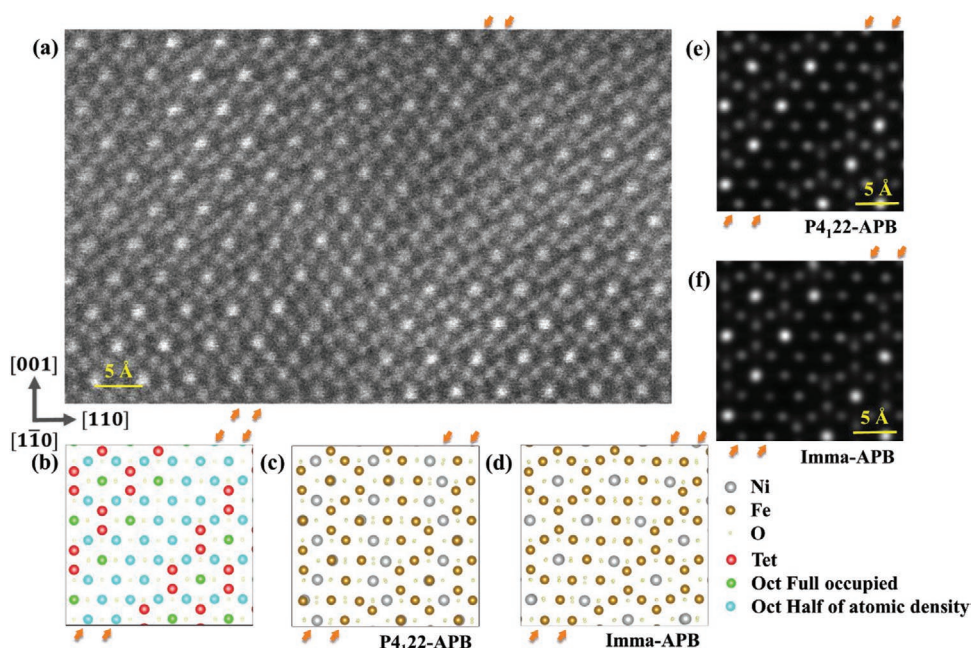
Dr. V. Kocevski
Materials Science and Technology Division
Los Alamos National Laboratory
Los Alamos, NM 87545, USA
Prof. H. Yanagihara, Prof. E. Kita
Department of Applied Physics
University of Tsukuba
Tsukuba, Ibaraki 3058573, Japan
Prof. H. Yanagihara
Tsukuba Research Center for Energy Materials Science (TREMS)
University of Tsukuba
Tsukuba, Ibaraki 3058573, Japan
Prof. J. Mayer
Central Facility for Electron Microscopy
RWTH Aachen University
52074 Aachen, Germany

2. Results and Discussion

2.1. Atomic Structure of Antiphase Boundary

Figure 1a shows a raw experimental HAADF STEM image of an APB in $NiFe_2O_4$ with an apparent crystal translation of $\pm(1/8)a[11\bar{2}]$ when viewed along the $[1\bar{1}0]$ direction. When considered together with a component of the crystal translation of $\pm(1/8)a[1\bar{1}0]$ that is not visible in the $[1\bar{1}0]$ direction, the total translation vector associated with this APB is either $\pm(1/4)a[101]$ or $\pm(1/4)a[011]$, as expected for spinel ferrites.[5b] Since APBs that have translations of $\pm(1/4)a[011]$ and $\pm(1/4)a[101]$ are crystallographically equivalent in spinel ferrites,[14] we refer only to a translation of $(1/4)a[011]$ below. It should be noted that only atomic columns that contain metal atoms are visible in the HAADF STEM image, as the oxygen atomic columns scatter the electron beam too weakly. Unlike the APBs that are more commonly seen in spinel ferrites, the two shifted domains in Figure 1a are not connected to each other directly, but are instead separated by a rock salt structure interlayer, as indicated by orange arrows.

In order to determine the atomic density of the metal atoms in this rock salt structure interlayer, we investigated the relationship between the atomic density and the intensities of atomic columns in both the APB interlayer and the perfect domains in the regions of the HAADF STEM image that are marked by colored dots in **Figure 2**a. The inverse spinel $NiFe_2O_4$ crystal structure has $Fd\bar{3}m$ symmetry, a face centered cubic oxygen array with Fe^{3+} ions distributed in one-eighth of the tetrahedral interstices and Ni^{2+} and Fe^{3+} ions distributed in half of the octahedral interstices. It can be described in the form $(Fe^{3+})_{tet}(Ni^{2+}Fe^{3+})_{oct}O_4$ for its nominal stoichiometric ratio. In an atomic model of perfectly-ordered $NiFe_2O_4$ viewed along the $[1\bar{1}0]$ direction (Figure S1e, Supporting Information), atomic columns along which the octahedral interstices are fully occupied by metal atoms (shown in green) have twice the atomic density of metal atoms compared to atomic columns along which only half of the octahedral interstices are occupied by metal atoms in an ordered manner (shown in blue). Figure S1a, Supporting Information, shows a representative HAADF STEM image of perfectly-ordered $NiFe_2O_4$ viewed along the $[1\bar{1}0]$ direction, in which atomic columns that have twice the atomic density are brighter than other atomic columns. The intensities of octahedral atomic columns in the HAADF STEM image, which increase monotonically with their atomic density,[15] were analyzed statistically, as shown in Figure 2b. (The intensity difference between Fe and Ni was not taken into account in this analysis, as a result of the close atomic numbers of the two elements). Figure 2b shows that average values of the normalized intensities of fully-occupied atomic columns in the perfect domains (in dimensionless units) are 1.00 ± 0.16 (red) and 0.97 ± 0.20 (green) on the left and right sides, respectively, while average values of the normalized intensities of atomic columns with half of the atomic density in the perfect domains are 0.56 ± 0.07 (blue) and 0.63 ± 0.08 (purple) on the left and right sides, respectively. In contrast, average values of the normalized intensities of atomic columns in the rock salt structure APB interlayer are 0.63 ± 0.15 (orange), that is, close to the intensities of atomic columns with half of the atomic density

2008306 (2 of 10)

Figure 1. Atomic structure of an individual rock salt structure antiphase boundary (APB) in $NiFe_2O_4$. a) Raw high-angle annular dark-field scanning transmission electron microscopy (HAADF STEM) image of an APB in $NiFe_2O_4$ viewed in the $[1\bar{1}0]$ direction. Orange arrows indicate the positions of two rock salt structure atomic interlayers. b) Atomic model of $NiFe_2O_4$ with an APB. Atomic columns with metal atoms fully and half occupying octahedral (Oct) interstices are shown in green and blue, respectively, while atomic columns with Fe atoms occupying tetrahedral (Tet) interstices are shown in red. c,d) Atomistic APB models of $NiFe_2O_4$ with c) $P4_122$ symmetry and d) Imma symmetry. e,f) Simulated HAADF STEM images calculated from the theoretical APB models for e) $P4_122$ symmetry and f) Imma symmetry.

in the perfect domains. It is therefore inferred that, on average, approximately half of the octahedral interstices in the rock salt structure interlayer are occupied by metal atoms, although the increased standard deviation of the normalized intensities in the rock salt structure APB interlayer suggests a higher degree of randomness of the occupied octahedral interstices when viewed along the $[1\bar{1}0]$ direction.

In order to validate the proposed model for this APB, in which half of the octahedral interstices are occupied within the interlayer, DFT calculations were used to fully relax the structure model. Two specific B-site orderings of $NiFe_2O_4$ were considered in DFT calculations, with either $P4_122$ (α-type) or Imma (β-type) symmetry instead of $Fd\bar{3}m$ symmetry, for the following reasons: First, short-range B-site ordering has been reported in inverse spinel $NiFe_2O_4$ using Raman spectroscopy.[16] Second, the presence of randomly-distributed octahedral Ni^{2+} and Fe^{3+} in $NiFe_2O_4$ with $Fd\bar{3}m$ symmetry could lead to thousands of possible configurations, making theoretical calculations unnecessarily complicated and impractical. In our previous work, calculations have shown that $NiFe_2O_4$ with $P4_122$ symmetry has the lowest system energy, whereas $NiFe_2O_4$ with Imma symmetry has a system energy that is only 3 meV/atom higher than that for $P4_122$ symmetry.[11a] Third, as a result of the close atomic numbers and scattering powers of Fe and Ni, there is no significant intensity difference in simulated Z-contrast HAADF STEM images when $Fd\bar{3}m$ symmetry is replaced by $P4_122$ or Imma symmetry. The validity of performing such structural replacements was confirmed by simulating HAADF STEM images of perfectly-ordered $NiFe_2O_4$ with $Fd\bar{3}m$ symmetry
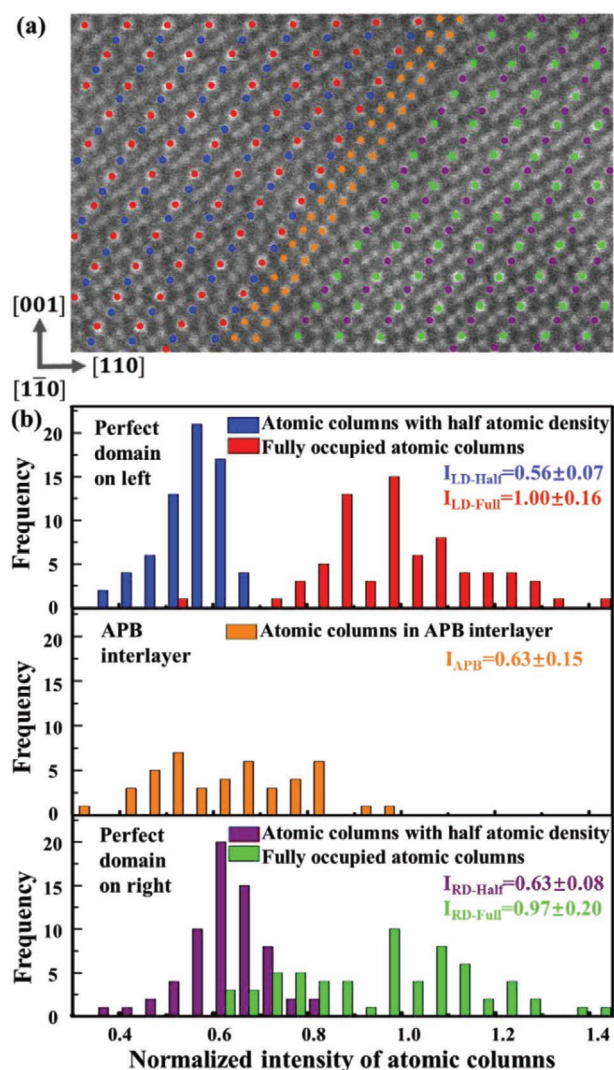
(Figure S1b,f, Supporting Information), $P4_122$ symmetry (Figure S1c,g) and Imma symmetry (Figure S1d,h).

The resulting DFT-relaxed atomistic models of the APB in $NiFe_2O_4$ are shown in Figure 1c,d for $P4_122$ and Imma symmetry, respectively. Figure 1e,f shows corresponding simulated HAADF STEM images. The positions of atomic columns in both simulated images are consistent with those in the experimental HAADF STEM image (Figure 1a), confirming the consistency of the rock salt structure APB model, with half of the octahedral interstices occupied in the interlayer. Remaining differences in the intensities of atomic columns in the interlayer between the simulated and experimental images are attributed to the use of ordered occupied octahedral interstices in the models, rather than randomly-occupied octahedral interstices.

2.2. Electron Magnetic Circular Dichroism of Antiphase Boundary

In order to investigate magnetic coupling at this APB with element specificity and high spatial resolution, EMCD experiments were performed in nanobeam mode using a probe size of 1.8 nm. A so-called two-beam case (2BC) orientation, with the (004) systematic reflection excited, was chosen for recording experimental EMCD spectra, as shown in the insets to **Figure 3**. The original EMCD spectra, which are shown in blue without smoothing, correspond to differences between normalized experimental electron energy-loss (EEL) spectra S_+ (black) and S_- (red) recorded at the positions "+" and "−", which are

**ADVANCED
SCIENCE NEWS**

www.advancedsciencenews.com

**ADVANCED
FUNCTIONAL
MATERIALS**

www.afm-journal.de

Figure 2. Atomic density analysis of the rock salt structure interlayers at the antiphase boundary (APB) in $NiFe_2O_4$. a) High-angle annular dark-field scanning transmission electron microscopy image of the APB, with colored dots corresponding to octahedral interstices. b) Statistical analysis of 72 fully-occupied atomic columns in red (average intensity $I_{LD-Full}$) and 67 atomic columns with half of the atomic density in blue (average intensity $I_{LD-Half}$) in the left perfect domain; statistical analysis of 44 atomic columns in the APB interlayer in orange (average intensity I_{APB}); statistical analysis of 63 fully-occupied atomic columns in green (average intensity $I_{RD-Full}$) and 65 atomic columns with half of the atomic density in purple (average intensity $I_{RD-Half}$) in the right perfect domain.

marked using white circles in the insets to Figure 3. The asymmetry of the non-magnetic contributions to the signal in EMCD experiments in a 2BC orientation can lead to different noise levels in S_+ and S_- spectra recorded using the same exposure time.[17] Figure 3 shows that Fe EMCD spectra recorded from the APB region and the adjacent perfect domains are associated with significant negative signals at the Fe L_3 edge and relatively weak positive signals at the Fe L_2 edge. Figure S2, Supporting Information, shows that Ni EMCD spectra recorded from the APB region and the adjacent perfect domains are associated

with very weak but measurable negative signals at the Ni L_3 edge and positive signals at the Ni L_2 edge. The cumulative sums of the Ni EMCD spectra from the APB region and the adjacent perfect domains (shown in green in Figure S2, Supporting Information) decrease under the L_3 edge and rise under the L_2 edge, further confirming the presence of negative and positive signals in the EMCD spectra at the Ni L_3 and L_2 edges, respectively. The L_3/L_2 white line ratios, which increase with Fe cation valence state, are shown in Figure S3d, Supporting Information[18] in the form of two isotropic spectra that were recorded from a perfect domain and the APB and normalized over the L_3 edge within the energy range from 704 to 717 eV. The resulting integration curve shows that the integral of the step-function-removed isotropic spectrum over the L_2 edge is smaller for the APB than for the perfect domains. The fact that the L_3/L_2 white line ratio recorded from the APB is higher than that from the perfect region indicates that the Fe ion valence state is higher in the APB area. However, under the current electron beam illumination conditions, shifts in binding energy could not be discerned.

When using convergent beam illumination, the spatial resolution of EMCD depends on the probe size, while the strength of the magnetic signal decreases with decreasing probe size. Because an electron probe with a diameter of only 1.8 nm was used for the detection of local magnetic properties at the present APB, the signal-to-noise ratio (SNR) in the EMCD spectra was relatively poor, albeit still within a reasonable range, especially when considering the relationship between SNR and illumination area in previous works.[13a] Quantitative analysis of the SNR and confidence level in the experimental EMCD spectra was performed using a method that is described by Thersleff et al.[13a] and explained in the Supporting Information. Gaussian curve fitting, as shown in yellow in Figure 3a,b, was used to evaluate the signal strength, which is defined by the peak value of the Gaussian curve. Noise values were calculated as standard deviations of EMCD spectra in the pre-edge and post-edge regions. The SNR was then defined as the ratio between the signal and noise estimates. The SNR values of the EMCD signals at the Fe L_3 edges in the perfect domain and the APB 2.16 and 1.67, respectively, corresponding to confidence levels of 96.92% and 90.50%. The SNR values of the EMCD signals at the Fe L_2 edges in the perfect domain and the APB are 0.38 and 1.50, respectively, corresponding to lower confidence levels of 29.60% and 86.64%. The relatively weak signals at the positions of the Fe L_2 edges may be attributed to a non-zero orbital magnetic moment, plural scattering and shorter core-hole lifetimes of excitations from $2p_{1/2}$ levels, as compared to $2p_{3/2}$ levels.[12c,19]

The EMCD intensities at both the L_3 and the L_2 edges were taken into account when quantitatively comparing experimental EMCD signals recorded from the APB and the perfect domains in terms of the normalized strength of the EMCD spectra NS_{emcd} (in units of eV), based on Equation (S24), Supporting Information

$$NS_{emcd} = 5\int_{L_3} (S_+ - S_-)_N \, dE - 4\int_{L_2} (S_+ - S_-)_N \, dE \qquad (1)$$

where $\int_{L_3}(S_+ - S_-)_N \, dE$ and $\int_{L_2}(S_+ - S_-)_N \, dE$ are integrals over normalized EMCD spectra at the L_3 and L_2 edges, respectively. NS_{emcd}
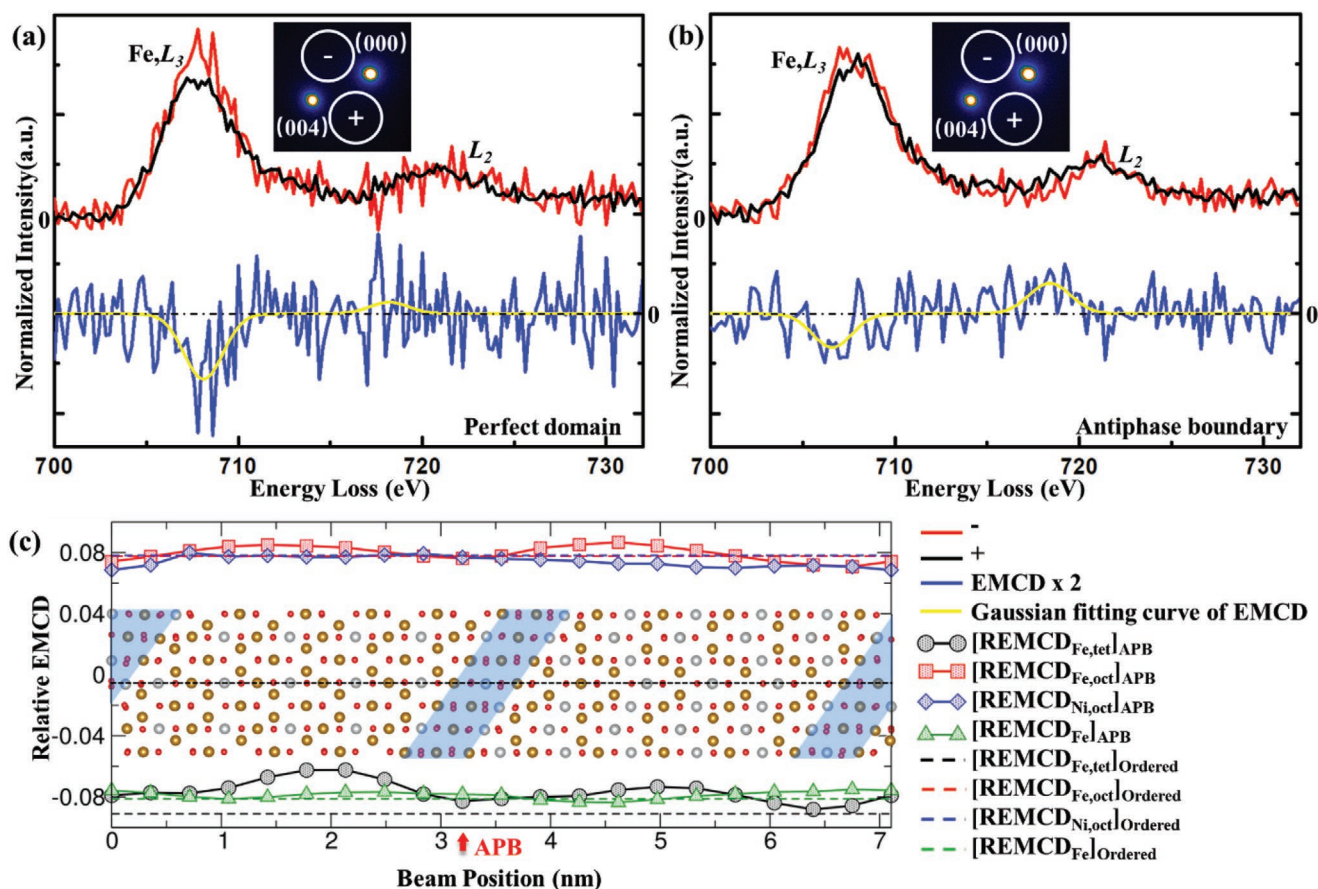
Figure 3. Normalized electron energy-loss spectra recorded from positive "+" (black) and negative "−" (red) positions, electron magnetic circular dichroism (EMCD) spectra (blue), and corresponding Gaussian curve fitting (yellow) for Fe in $NiFe_2O_4$ at a) a perfect domain and b) an APB. (004) two-beam condition and detector positions are shown in the insets. c) Calculated electron-beam-position-dependent strengths of the relative EMCD (REMCD) coefficients for each atom in the APB interlayer and perfectly-ordered $NiFe_2O_4$, on the assumption that Fe and Ni atoms in the octahedral interstices do not change their electronic structure, magnetic moment direction, or strength within the APB interlayer, compared to perfectly-ordered $NiFe_2O_4$. The simulated electron beam scans along the dashed black line in the middle of the $P4_122$ − APB atomic model, with the position of the APB shadowed in blue. Coefficients for Fe ($REMCD_{Fe}$) are a weighted sum of the corresponding coefficients Fe_{tet} and Fe_{oct}.

for Fe was measured to be -0.26 ± 0.04 and -0.14 ± 0.01 in the perfect domains and the APB, respectively, whereas for Ni it was estimated to be -0.91 ± 0.14 and -0.56 ± 0.10 in the perfect domains and the APB, respectively. Considering the relatively low SNR in the Ni EMCD spectra, there is a reduction of approximately $46.8\% \pm 8.2\%$ and $38.8\% \pm 14.5\%$ in normalized strength for the Fe and Ni EMCD signals, respectively, in the APB when compared to values measured in the perfect domains. A detailed description of the process of error estimation and confidence level calculation is presented in the Supporting Information. It should be noted that the low signal of the Fe L_2 edge in the perfect domains may lead to an underestimation of the contribution from the Fe L_2 edge to NS_{emcd} for the perfect domains, suggesting that the actual value of NS_{emcd} may be even larger for the perfect domains and may lead to an even greater reduction in experimental EMCD signals.

The experimental EMCD strengths are determined by the intrinsic magnetic moments and dynamical diffraction coefficients of each atom in the material. In order to quantitatively evaluate the influence of the dynamical diffraction coefficients, beam-position-dependent dynamical diffraction calculations

based on the DFT-relaxed APB model were performed to predict experimental EMCD strengths on the assumption that the Fe and Ni atoms in the octahedral interstices do not change their electronic structure, magnetic moment direction, or strength inside the APB interlayer, when compared to the Fe and Ni atoms in the octahedral interstices in the perfectly-ordered region of $NiFe_2O_4$. Under this assumption, the normalized strengths of the EMCD spectra are proportional to the calculated strengths of the relative EMCD (REMCD) coefficients (in dimensionless units), as shown in the Supporting Information. The REMCD strengths of Fe and Ni in perfectly-ordered $NiFe_2O_4$ were calculated to be -8.4% and 7.8%, respectively, as indicated by dashed green and blue lines in Figure 3c. Absolute numbers for REMCD coefficients in the APB region are taken at the position marked by a red arrow on the horizontal axis. The calculated REMCD strengths of Fe and Ni in the APB region are found to be -7.9% and 7.7%, respectively, as indicated by green triangles and blue diamonds in Figure 3c. The standard deviations of all of the REMCD strengths for Fe (green triangles) and Ni (blue diamonds), as shown in Figure 3c, are only $\approx 0.3\%$, indicating that both the rock salt structure in the
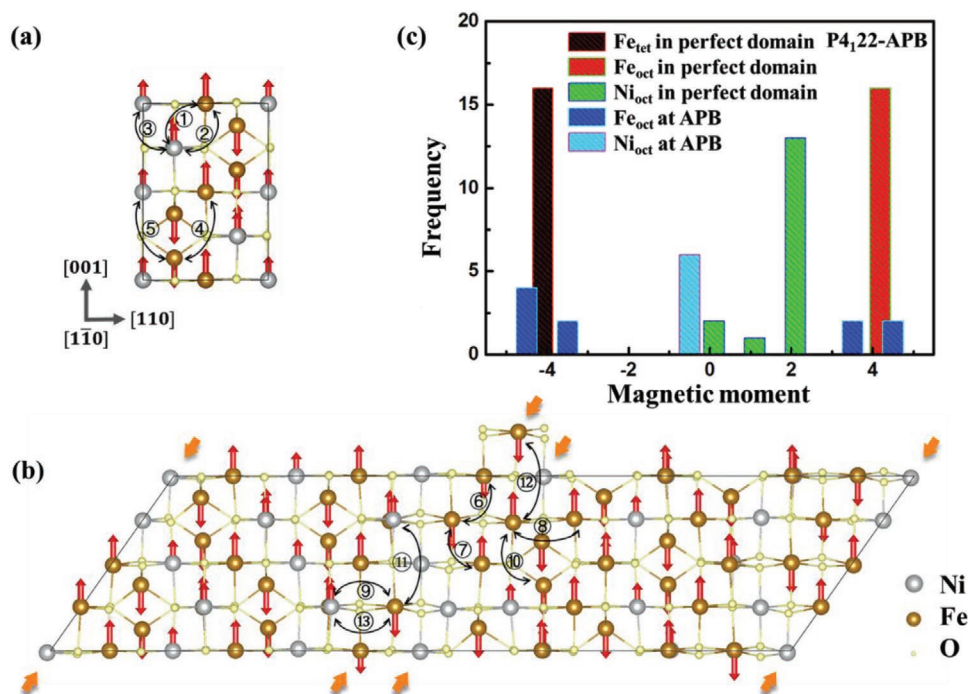
Figure 4. First-principles density functional theory magnetic calculations for $NiFe_2O_4$ for a) a pure $P4_122$ structure and b) a $P4_122 - APB$ structure. c) Magnetic moment histogram for atoms in the $P4_122 - APB$ model. The rock salt structure atomic interlayers at the APB are marked by orange arrows. The circled numbers indicate the positions of exchange parameters (J) between magnetic pairs. The lengths of the red arrows represent the magnitudes of the magnetic moments, while their directions are obtained from calculated exchange parameters (J). The lengths of the arrows for Ni are magnified by a factor of two for better visibility.

APB and the inverse spinel structure in the perfect domains satisfy similar optimized diffracting conditions and result in comparable REMCD strengths in the experimental geometry. Considering that the theoretically-predicted NS_{emcd} is proportional to the calculated $REMCD$ strength, the NS_{emcd} is predicted to be approximately the same in the APB as in perfectly-ordered $NiFe_2O_4$, in contradiction to the experimental results. Therefore, the initial assumption that was made in the simulations is necessarily incorrect, suggesting that the Fe and Ni atoms in the APB region have different electronic structures, or different magnitudes and/or directions of magnetic moment, when compared to atoms in perfectly-ordered $NiFe_2O_4$.

2.3. Magnetic Coupling at Antiphase Boundary

In order to understand the physical origin of the reduced EMCD strength in the APB region, first-principles DFT calculations[19,20] were performed. Both α-type ($P4_122$) and β-type (Imma) B-site ordering structures were considered in DFT + U calculations. The plausibility of these crystallographic structures was discussed above with reference to HAADF STEM simulations. Further support for these structures, based on DFT calculations, is provided below (for $P4_122$ symmetry) and in the Supporting Information (for Imma symmetry).

In perfectly-ordered $NiFe_2O_4$ that has $P4_122$ symmetry, there are five kinds of interactions between pairs of nearest neighbor magnetic ions that are connected by oxygen anions: $90°$-Fe_{oct}—O—Fe_{oct}, $90°$-Fe_{oct}—O—Ni_{oct}, $90°$-Ni_{oct}—O—Ni_{oct},

$120°$-Fe_{tet}—O—Fe_{oct} and $120°$-Fe_{tet}—O—Ni_{oct} (**Figure 4**, **Table 1**), where Fe_{tet}, Fe_{oct}, and Ni_{oct} represent Fe ions in tetrahedral interstices, and Fe and Ni ions in octahedral interstices, respectively. $90°$ interactions are formed between magnetic ions on octahedral sites, whereas $120°$ interactions are formed between magnetic ions on tetrahedral sites and magnetic ions on octahedral

Table 1. Exchange parameters (J) (in eV) for the $P4_122$ structure with an antiphase boundary ($P4_122 - APB$).

	Angle	Number[a]	Atom$_1$	Atom$_2$	J [eV]
Ordered	90°	1	Fe_{oct}	Fe_{oct}	0.0012
		2	Fe_{oct}	Ni_{oct}	−0.0014
		3	Ni_{oct}	Ni_{oct}	−0.0012
	120°	4	Fe_{tet}	Fe_{oct}	0.0352
		5	Fe_{tet}	Ni_{oct}	0.0178
APB	90°	6	Fe_{oct}	Fe_{oct}	−0.0014
		7	Fe_{oct}	Fe_{oct}	0.0326
		8	Fe_{oct}	Fe_{oct}	0.0067
		9	Fe_{oct}	Fe_{oct}	0.0040
	120°	10	Fe_{tet}	Fe_{oct}	0.0565
	170°	11	Fe_{oct}	Fe_{oct}	0.0339
		12	Fe_{oct}	Fe_{oct}	0.0190
		13	Fe_{oct}	Ni_{oct}	0.0276

[a]The sequence number corresponds to that indicated in Figure 4.

**ADVANCED
SCIENCE NEWS**

www.advancedsciencenews.com

**ADVANCED
FUNCTIONAL
MATERIALS**

www.afm-journal.de

sites. Interactions of the five magnetic pairs were analyzed using a four-state method.[21] We adopted the Heisenberg spin Hamiltonian $H_{spin} = \sum_{i<j} J_{ij} \hat{S}_i \cdot \hat{S}_j$, where J_{ij} are exchange coupling parameters and $\hat{S}_i$ represents a spin moment vector at site i. In our work, a negative value of J corresponds to ferromagnetic coupling. Calculated exchange parameters (J) are given in Table 1. Strong antiferromagnetic coupling is present for both of the 120° interactions, with magnitudes of 0.0352 and 0.0178 eV for 120°-Fe_{tet}—O—Fe_{oct} and 120°-Fe_{tet}—O—Ni_{oct}, respectively. 90° interactions with Ni^{2+} on the octahedral sites tend to couple ferromagnetically, with magnitudes of −0.0014 and −0.0012 eV for 90°-Fe_{oct}—O—Ni_{oct} and 90°-Ni_{oct}—O—Ni_{oct}, respectively. In contrast, 90° interactions between Fe^{3+} tend to be weakly antiferromagnetic (0.0012 eV), in agreement with the Goodenough–Kanamori rule.[22] All 90° interactions between octahedral sites are much weaker than 120° interactions, by approximately an order of magnitude. The overall magnetic coupling in the $P4_122$ $NiFe_2O_4$ structure therefore remains the same as that in $Fd\bar{3}m$ $NiFe_2O_4$, in which magnetic ion on octahedral sites couple antiferromagnetically to magnetic ion on tetrahedral sites.

Figure 4c shows a histogram of the magnetic moments of Fe atoms and Ni atoms in the $P4_122 – APB$ model based on a statistical analysis of their magnitudes and directions, as indicated by red arrows in Figure 4b. In perfect domains in the $P4_122 – APB$ model, Fe ions in tetrahedral interstices are antiferromagnetically coupled with Fe and Ni atoms in octahedral interstices, as expected, while the magnitudes of the magnetic moments of the Fe atoms in both the octahedral and the tetrahedral interstices are almost identical. Some Ni atoms in the perfect domains adjacent to the APB have lower magnitudes of their magnetic moments, when compared with other Ni atoms in the perfect domains. Furthermore, the magnetic moments of the Ni ions decrease from 1.6 μ_B in the perfectly-ordered domains to approximately −0.1 μ_B in the rock salt structure APB interlayer, which partly explains the decreased Ni EMCD signals at the APB. The vanishingly small local magnetic moment and the smaller radii of the Ni ions near the APB implies that these Ni ions take the form of low-spin Ni^{4+} (d^6) ions. Coupling between Fe atoms in the rock salt structure interlayer is antiferromagnetic. When compared to Fe atoms in perfect domains of the $P4_122 – APB$ model (Figure 4b,c), most of the Fe atoms in the APB have nearly unchanged magnitudes of their magnetic moments, while some Fe atoms have slightly lower values as a result of the presence of Fe^{4+} ions in the rock salt structure interlayer, as confirmed theoretically in projected densities of states (PDOS). Plots of the PDOS for Fe and Ni ions in the perfect domain and APB interlayer can be found in Figure S4, Supporting Information. For Fe ions, the spin-down e_g orbitals are partly occupied, with some e_g lying above the Fermi level, corresponding to a reduced number of valence electrons at the Fe atoms in the APB interlayer and resulting in an Fe^{4+} valence state (the local magnetic moment is 3.1 μ_B). For Ni ions, the t_{2g} orbitals are fully occupied and the e_g orbitals are empty, meaning that Ni ions in the APB interlayer have very small magnetic moments.

At the APB, two types of 90° magnetic interactions were considered in the two interlayers with rock salt structures. When the magnetic ions are located on the same {111} plane,

the 90°-Fe_{oct}—O—Fe_{oct} interactions are weakly ferromagnetic (−0.0014 eV). However, when the magnetic ions come from different {111} planes, the 90°-Fe_{oct}—O—Fe_{oct} interactions are strongly antiferromagnetic (0.0326 eV). In a region of the perfect domain that is closest to the APB, 90°-Fe_{oct}—O—Fe_{oct} from different {111} planes remain weakly antiferromagnetically coupled (0.0067 and 0.0040 eV), yet 120°-Fe_{tet}—O—Fe_{oct} tend to be coupled antiferromagnetically even more strongly (0.0565 eV) when compared to the perfect domain. More importantly, cations on octahedral sites in the two rock salt structure {111} layers also couple antiferromagnetically to cations on octahedral sites in the $(11\bar{1})$ layers in the adjacent perfect domains (Figure 4b). The insertion of rock salt structure interlayers also leads to a new type of magnetic coupling (termed 170°-Fe_{oct}—O—Fe_{oct}/ Ni_{oct}, as the Fe_{oct}—O—Fe_{oct}/Ni_{oct} angle is ≈170°). The DFT calculations suggest rather strong antiferromagnetic coupling for the 170° magnetic interaction, which agrees with the Goodenough–Kanamori rule (whereby the 180°-Fe_{oct}—O—Fe_{oct} spin exchange is predicted to be strongly antiferromagnetic).[22] It results in antiferromagnetic coupling between cations that are located on two neighboring rock salt structure {111} planes. The antiferromagnetic coupling between the Fe ions on the octahedral sites leads to a significant decrease in Fe EMCD signal strength recorded from the APB region. The magnetic structure of the $P4_122 – APB$ model deduced from calculated exchange parameters (J) in Figure 4b is the most stable structure with the lowest energy, when compared with other magnetic structures considered in Figure S5, Supporting Information.

The magnetic interactions (Figure S8 and Table S1, Supporting Information) and the lowest magnetic states (Figure S9, Supporting Information) of $NiFe_2O_4$ in the $Imma$ perfect domain and the $Imma – APB$ model are discussed in detail in the Supporting Information. Similarly, the local magnetic moments of the Ni ions in the APB interlayer decrease by almost 50% as a result of their change to low-spin state Ni^{4+} (d^6) ions. The insertion of rock salt structure layers here also leads to the introduction of strongly antiferromagnetic 170°-Fe_{oct}—O—Ni_{oct} interactions, which result in antiferromagnetic coupling between Fe ions in the inserted {111} planes and therefore a decreased Fe EMCD signal from the APB region. We also analyzed the PDOS of the $Imma–APB$ structure (Figure S4, Supporting Information) and obtained the same conclusions.

It is worth noting that an APB with a rock salt structure potentially has a Néel temperature that is very close to or higher than room temperature, given that FeO and NiO have Néel temperatures of 198 and 523 K, respectively. In AFM/FM or FM/AFM/FM heterostructures, the ordering temperature of the AFM interlayer can be enhanced significantly or influenced by the neighboring FM layer due to the magnetic proximity effect.[23] In the present case, $NiFe_2O_4$ has a Curie temperature of 865 K, which is much higher than room temperature.[24] Taking magnetic proximity effects into account, an APB with a rock salt structure buried between adjacent ferrimagnetic $NiFe_2O_4$ grains is likely to have a Néel temperature above room temperature. Studies of the Néel temperature of the APB and its effects on the local magnetization are planned for future temperature-dependent experiments and theoretical calculations.

**ADVANCED
SCIENCE NEWS**

www.advancedsciencenews.com

**ADVANCED
FUNCTIONAL
MATERIALS**

www.afm-journal.de

3. Conclusions

High-spatial-resolution EMCD and HAADF STEM imaging have been used to experimentally demonstrate reductions of 46.8% ± 8.2% and 38.8% ± 14.5% in the EMCD strengths of Fe and Ni, respectively, at a new type of APB in $NiFe_2O_4$ that has a rock salt structure and a relative translation of $(1/4)a[011]$, compared to perfectly-ordered $NiFe_2O_4$. DFT calculations and dynamical diffraction calculations suggest that the reduced EMCD strengths result from the fact that Fe ions at the APB interlayer are antiferromagnetically coupled with each other, whereas Ni ions show a significant decrease in magnetic moment as a result of the formation of low-spin state Ni^{4+} (d^6) ions. Intensity analysis of octahedral atomic columns in HAADF STEM images suggests that only half of the octahedral interstices in the rock salt structure interlayer are occupied. Such local magnetic information with element specificity is crucial for understanding magnetic coupling within the APB. Our combined approach of using high-spatial-resolution EMCD and first-principles calculations to resolve and identify the atomic structure and magnetic coupling of an individual APB in spinel ferrite is applicable to studies of a broad spectrum of other defects in magnetic materials.

4. Experimental Section

$NiFe_2O_4$ thin films were fabricated on $MgAl_2O_4$ substrates using reactive radio frequency magnetron sputtering. The $MgAl_2O_4$ substrates were first annealed at 400 °C for 30 min under vacuum prior to deposition. After 10 min of pre-sputtering, the nickel ferrite films were deposited at a substrate temperature of 300 °C.[25]

Cross-sectional TEM samples were prepared using an FEI Helios NanoLab 400S FIB SEM.[26] Atomic-resolution HAADF STEM images were recorded at 200 kV in an FEI Titan G2 80–200 ChemiSTEM microscope[27] with a beam convergence semi-angle of ≈17.7 mrad and collection semi-angles ranging from 70 to 200 mrad. These experimental parameters were also used to perform HAADF STEM image simulations using Dr Probe software[28] for 188 projected potential slices and 47 unit cells in the $[1\bar{1}0]$ direction, without introducing any aberrations and with 20 variants per slice in frozen-lattice configurations. The image simulations were convoluted by a Gaussian function to take into account partial spatial coherence using a probe with a half width at half-maximum of 0.04 nm. Quantitative HAADF STEM intensity profiles were extracted with an integration width of 10 pixels, corresponding to 0.09 nm in real space, using Digital Micrograph software. Background subtraction and Gaussian function fitting were employed before integration over 0.05 nm of the intensity profiles for each atomic column.[29] All of the intensities were normalized to the average intensities of fully-occupied atomic columns in the perfect grain on the left side of the APB.

EEL spectra and EMCD experiments were performed under nanobeam illumination at 300 kV using an FEI Titan 80–300 STEM[30] with an energy resolution of ≈1.2 eV, a beam full width at half maximum (FWHM) of ≈1.8 nm,[12f] a collection semi-angle of ≈3.72 mrad and a convergence semi-angle of ≈0.65 mrad. In order to track the same APB using atomic-scale imaging and in nanobeam mode, four auxiliary holes were drilled on the nanometer scale using the electron beam. EMCD signals from the APB were recorded at the intersection of connecting lines between holes 1 and 3 and holes 2 and 4 (Figure S10, Supporting Information). Background subtraction, deconvolution of plural scattering, and post-edge normalization were performed during EELS data processing. The $\int_{L_3+L_2} (S_+ + S_-)dE$ term, after subtracting a step function,[31] was used for

normalizing the spectra between the ordered area and the APB. The integration ranges used were 704–717 eV for the Fe L_3 edge, 717–731 eV for the Fe L_2 edge, 849–861 eV for the Ni L_3 edge, and 866–878 eV for the Ni L_2 edge. The sample thickness was measured using low-loss EEL spectra.

Structural relaxation and electronic structure calculations were carried using DFT methods with the Vienna ab initio simulation package (VASP)[32] with the projector-augmented-wave (PAW) method.[33] The Perdew-Burke–Ernzerhof functional of the generalized gradient approximation (GGA–PBE function)[34] was used to describe the exchange-correlation energy. In order to better describe strong electron–electron correlations, the GGA with on-site Coulomb repulsion U (GGA+U) method was adopted.[35] The value of the effective on-site repulsion U was set to be 4 and 4.5 eV for Ni and Fe ions, respectively, in agreement with previous work.[36] The spin exchange interaction parameters were computed using U_{eff} = 4.0 and 3.0 eV for Ni and Fe ions, respectively,[37] and similar results were obtained (see Table S2, Supporting Information). The energy cutoff and convergence criteria for total energy and forces were set to be 400, 10^{-6}, and 0.01 eV $Å^{-1}$, respectively. Further computational details are given in the Supporting Information. For the structural model with APBs, a supercell containing two APBs in the [110] direction was constructed to fulfill periodic boundary conditions. With the available computational resources, only a distance of 15 Å between adjacent APBs could be taken into consideration. In the present structure model, the distances between periodic images of individual magnetic atoms were more than 10 Å, which should lead to negligible interactions between them. The supercell contained 640 atoms and its cell parameters were a = 35.58 Å, b = 20.47 Å, c = 11.84 Å. All of the atom positions in the structure models were fully relaxed. For the purpose of more intuitive visualization, only the original $P4_122$ and Imma structures containing 28 atoms, and $P4_122$ − APB and Imma − APB supercells containing 160 atoms, are shown in Figure 4 and Figure S8, Supporting Information. During calculation of the exchange parameters J, the $P4_122$ and Imma cells were doubled along the $[1\bar{1}0]$, [110] and [001] directions, while the $P4_122$ − APB and Imma − APB cells were doubled along the $[1\bar{1}0]$ and [001] directions, in order to ensure a distance of more than 10 Å between periodic copies of individual magnetic atoms.

EMCD simulations of the beam-position-dependent strength of EMCD and the non-magnetic part of the inelastic scattering cross-section were performed using MATS.v2 software[38] separately for the tetrahedral and octahedral sites and for both the Fe and the Ni 2p core-level excitations. The DFT-relaxed atomistic APB model with a distance of 29 Å between adjacent APBs for $NiFe_2O_4$ with $P4_122$ symmetry was used for the construction of a large orthogonal supercell consisting of 3936 atoms, with dimensions of 7.1 nm × 10.1 nm × 0.6 nm. The simulation parameters were chosen to match the experimental parameters, including accelerating voltage, convergence semi-angle, and probe size. The MATS.v2 summation convergence parameter was set to 2×10^{-5}. The beam scanning step across the APB was set to 0.5 nm.

Supporting Information

Supporting Information is available from the Wiley Online Library or from the author.

2008306 (8 of 10)

Conflict of Interest

The authors declare no conflict of interest.

Data Availability Statement

The data that supports the findings of this study are available in the supplementary material of this article.

[1] Y. Suzuki, *Annu. Rev. Mater. Res.* **2001**, *31*, 265.

[2] a) H. C. Wu, M. Abid, B. S. Chun, R. Ramos, O. N. Mryasov, I. V. Shvets, *Nano Lett.* **2010**, *10*, 1132; b) R. G. S. Sofin, S. K. Arora, I. V. Shvets, *Phys. Rev. B* **2011**, *83*, 134436.

[3] D. T. Margulies, F. T. Parker, M. L. Rudee, F. E. Spada, J. N. Chapman, P. R. Aitchison, A. E. Berkowitz, *Phys. Rev. Lett.* **1997**, *79*, 5162.

[4] a) A. V. Singh, B. Khodadadi, J. B. Mohammadi, S. Keshavarz, T. Mewes, D. S. Negi, R. Datta, Z. Galazka, R. Uecker, A. Gupta, *Adv. Mater.* **2017**, *29*, 1701222; b) T. Niizeki, Y. Utsumi, R. Aoyama, H. Yanagihara, J.-i. Inoue, Y. Yamasaki, H. Nakao, K. Koike, E. Kita, *Appl. Phys. Lett.* **2013**, *103*, 162407.

[5] a) T. Hibma, F. C. Voogt, L. Niesen, P. A. A. van der Heijden, W. J. M. de Jonge, J. J. T. M. Donkers, P. J. van der Zaag, *J. Appl. Phys.* **1999**, *85*, 5291; b) S. Celotto, W. Eerenstein, T. Hibma, *Eur. Phys. J. B* **2003**, *36*, 271; c) K. P. McKenna, F. Hofer, D. Gilks, V. K. Lazarov, C. Chen, Z. Wang, Y. Ikuhara, *Nat. Commun.* **2014**, *5*, 5740.

[6] a) T. Kasama, R. E. Dunin-Borkowski, W. Eerenstein, *Phys. Rev. B* **2006**, *73*, 104432; b) Y. Murakami, K. Niitsu, T. Tanigaki, R. Kainuma, H. S. Park, D. Shindo, *Nat. Commun.* **2014**, *5*, 4133.

[7] Y. Murakami, K. Yanagisawa, K. Niitsu, H. S. Park, T. Matsuda, R. Kainuma, D. Shindo, A. Tonomura, *Acta Mater.* **2013**, *61*, 2095.

[8] C. Chen, H. Li, T. Seki, D. Yin, G. Sanchez-Santolino, K. Inoue, N. Shibata, Y. Ikuhara, *ACS Nano* **2018**, *12*, 2662.

[9] P. Schattschneider, S. Rubino, C. Hébert, J. Rusz, J. Kuneš, P. Novák, E. Carlino, M. Fabrizioli, G. Panaccione, G. Rossi, *Nature* **2006**, *441*, 486.

[10] P. J. Herbert, P. Window, C. J. Ackerson, K. L. Knappenberger, *J. Phys. Chem. Lett.* **2019**, *10*, 189.

[11] a) Z. Q. Wang, X. Y. Zhong, R. Yu, Z. Y. Cheng, J. Zhu, *Nat. Commun.* **2013**, *4*, 1395; b) Z. Wang, A. H. Tavabi, L. Jin, J. Rusz, D. Tyutyunnikov, H. Jiang, Y. Moritomo, J. Mayer, R. E. Dunin-Borkowski, R. Yu, J. Zhu, X. Zhong, *Nat. Mater.* **2018**, *17*, 221; c) D. Song, Z. Wang, J. Zhu, *Ultramicroscopy* **2019**, *201*, 1.

[12] a) P. Schattschneider, M. Stöger-Pollach, S. Rubino, M. Sperl, C. Hurm, J. Zweck, J. Rusz, *Phys. Rev. B* **2008**, *78*, 104413; b) D. Song, L. Ma, S. Zhou, J. Zhu, *Appl. Phys. Lett.* **2015**, *107*, 042401; c) L. Jin, C.-L. Jia, I. Lindfors-Vrejoiu, X. Zhong, H. Du, R. E. Dunin-Borkowski, *Adv. Mater. Interfaces* **2016**, *3*, 1600414; d) P.-L. Ho, C.-P. Yu, Q. Zhang, K. Song, J. P. Buban, S.-Y. Choi, R. E. Dunin-Borkowski, J. Mayer, N.-H. Tai, J. Zhu, L. Jin, X. Zhong, *Ultramicroscopy* **2018**, *193*, 137; e) X. Chen, S. Higashikozono, K. Ito, L. Jin, P.-L. Ho, C.-P. Yu, N.-H. Tai, J. Mayer, R. E. Dunin-Borkowski, T. Suemasu, X. Zhong, *Ultramicroscopy* **2019**, *203*, 37; f) J. Salafranca, J. Gazquez, N. Pérez, A. Labarta, S. T. Pantelides, S. J. Pennycook, X. Batlle, M. Varela, *Nano Lett.* **2012**, *12*, 2499.

[13] a) T. Thersleff, J. Rusz, B. Hjörvarsson, K. Leifer, *Phys. Rev. B* **2016**, *94*, 134430; b) J. Rusz, S. Muto, J. Spiegelberg, R. Adam, K. Tatsumi, D. E. Bürgler, P. M. Oppeneer, C. M. Schneider, *Nat. Commun.* **2016**, *7*, 12672.

[14] S.-B. Mi, R.-Y. Zhang, L. Lu, M. Liu, H. Wang, C.-L. Jia, *Acta Mater.* **2017**, *127*, 178.

[15] S. J. Pennycook, P. D. Nellist, *Scanning Transmission Electron Microscopy: Imaging and Analysis*, Springer, New York, NY **2011**.

[16] V. G. Ivanov, M. V. Abrashev, M. N. Iliev, M. M. Gospodinov, J. Meen, M. I. Aroyo, *Phys. Rev. B* **2010**, *82*, 024104.

[17] J. Rusz, P. Oppeneer, H. Lidbaum, S. Rubino, K. Leifer, *J. Microsc.* **2010**, *237*, 465.

[18] Y. Zhang, W. Wang, W. Xing, S. Cheng, S. Deng, M. Angst, C.-P. Yu, F. Lan, Z. Cheng, D. Mandrus, B. Sales, J. Shen, X. Zhong, N.-H. Tai, R. Yu, J. Zhu, *Phys. Rev. Lett.* **2019**, *123*, 247601.

[19] S. J. Blundell, I. M. Marshall, F. L. Pratt, M. A. Hayward, E. J. Cussen, J. B. Claridge, M. Bieringer, C. J. Kiely, M. J. Rosseinsky, *Phys. B* **2003**, *326*, 527.

[20] C. A. Bridges, G. R. Darling, M. A. Hayward, M. J. Rosseinsky, *J. Am. Chem. Soc.* **2005**, *127*, 5996.

[21] a) P. Novák, J. Rusz, *Phys. Rev. B* **2005**, *71*, 184433; b) H. Xiang, C. Lee, H.-J. Koo, X. Gong, M.-H. Whangbo, *Dalton Trans.* **2013**, *42*, 823.

[22] J. B. Goodenough, *Magnetism and the Chemical Bond*, John Wiley & Sons, New York, NY **1963**.

[23] a) Y. H. Lee, I. Song, S. H. Kim, J. H. Park, S. O. Park, J. H. Lee, Y. Won, K. Cho, S. K. Kwak, J. H. Oh, *Adv. Mater.* **2020**, *32*, 2070238; b) K. Lenz, S. Zander, W. Kuch, *Phys. Rev. Lett.* **2007**, *98*, 237201.

[24] J. M. D. Coey, *Magnetism and Magnetic Materials*, Cambridge University Press, Cambridge, UK **2010**.

[25] J. Morishita, T. Niizeki, K. Z. Suzuki, H. Yanagihara, E. Kita, *IEEE Trans. Magn.* **2014**, *50*, 1.

[26] D. Meertens, M. Kruth, K. Tillmann, *J. Large-Scale Res. Facilities* **2016**, *2*, A60.

[27] A. Kovács, R. Schierholz, K. Tillmann, *J. Large-Scale Res. Facilities* **2016**, *2*, A43.

[28] J. Barthel, *Ultramicroscopy* **2018**, *193*, 1.

[29] Y. Kotaka, *Ultramicroscopy* **2010**, *110*, 555.

[30] M. Heggen, M. Luysberg, K. Tillmann, *J. Large-Scale Res. Facilities* **2016**, *2*, A42.

[31] D. H. Pearson, C. C. Ahn, B. Fultz, *Phys. Rev. B* **1993**, *47*, 8471.

[32] G. Kresse, J. Furthmüller, *Comput. Mater. Sci.* **1996**, *6*, 15.

[33] G. Kresse, D. Joubert, *Phys. Rev. B* **1999**, *59*, 1758.

[34] J. P. Perdew, K. Burke, M. Ernzerhof, *Phys. Rev. Lett.* **1996**, *77*, 3865.

[35] V. I. Anisimov, F. Aryasetiawan, A. I. Lichtenstein, *J. Phys.: Condens. Matter* **1997**, *9*, 767.

[36] a) V. N. Antonov, B. N. Harmon, A. N. Yaresko, *Phys. Rev. B* **2003**, *67*, 024417; b) Z. Szotek, W. M. Temmerman, D. Ködderitzsch, A. Svane, L. Petit, H. Winter, *Phys. Rev. B* **2006**, *74*, 174431.

[37] a) S. Mehmood, Z. Ali, I. Khan, I. Ahmad, *Mater. Chem. Phys.* **2017**, *196*, 222; b) S. Mehmood, Z. Ali, I. Khan, I. Ahmad, *J. Electron. Mater.* **2020**, *49*, 3780.

[38] J. Rusz, *Ultramicroscopy* **2017**, *177*, 20.